Indentation strength of ultraincompressible rhenium boride, carbide, and nitride from first-principles calculations

Chenpeng Zang, Hong Sun, John S. Tse, and Changfeng Chen

Phys. Rev. B **86**, 014108 — Published 16 July 2012

DOI: 10.1103/PhysRevB.86.014108

Indentation strength of ultra-incompressible rhenium boride, carbide and nitride from first-principles calculations

Chenpeng Zang,[1] Hong Sun,[1,2,*] John S. Tse,[3] and Changfeng Chen[2,†]

[1]*Department of Physics, Shanghai Jiao Tong University, Shanghai 200240, and Key Laboratory of Artificial Structures and Quantum Control, Ministry of Education, China*
[2]*Department of Physics and High Pressure Science and Engineering Center, University of Nevada, Las Vegas, Nevada 89154, USA*
[3]*Department of Physics and Engineering Physics, University of Saskatchewan, SK S7N 5E2, Canada*

(Dated: June 27, 2012)

Using a recently developed first-principles approach for determining indentation strength [Phys. Rev. Lett. **98**, 135505 (2007); *ibid*, **102**, 055503 (2009)], we performed calculations of the ideal strength of hexagonal Re, Re_3N, Re_2N, Re_2C, Re_2B and ReB_2 in various shear deformation directions beneath the Vickers indentor. Our results show that the normal compressive pressure beneath the indentor weakens the strength of these electron-rich rhenium boride, carbide and nitride compounds which belong to a distinct class of ultra-incompressible and ultrahard materials. The reduction of indentation strength in these materials stems from lateral bond and volume expansions driven by the normal compressive pressure mediated by the high-density valence electrons in these structures. We compare the calculated indentation strength to the Poisson's ratio, which measures the lateral structural expansion, for the rhenium boride, carbide and nitride compounds as well as diamond and cubic boron nitride. Our analysis indicates that although the normal pressure beneath the indentor generally leads to more significant reduction of indentation strength in materials with larger Poisson's ratios, crystal and electronic structures also play important roles in determining the structural response under indentation. The present study reveals structural deformation modes and the underlying atomistic mechanisms in transition-metal boride, carbide and nitride compounds under the Vickers indentation. The results are distinctive from those of the traditional covalent superhard materials. The insights obtained from this work have important implications for further exploration and design of ultrahard materials.

PACS numbers: 62.20.-x, 81.40.Jj

I. I. INTRODUCTION

The search for materials with superior mechanical strength or hardness has been one of the long-standing and most active research fields in materials science. These so-called superhard materials like diamond and cubic boron nitride (c-BN) are traditionally formed under extremely high-pressure conditions which make their synthesis expensive. Therefore, recent synthesis of hexagonal rhenium diboride (ReB_2) under ambient pressure is considered a breakthrough and has reignited great interest in the synthesis and study of this class of metallic ultra-incompressible materials proposed decades ago.[1–19] The synthesis of these materials follow the design principle[1,2,4] that combines small, light covalent elements (B, C, N and O) with large, electron-rich transition metals (Ta, W, Re, Os, Ru, Ir, Pt, $\cdots$), based on the idea that covalent elements form strong, directional covalent bonds with the transition metals, while the high density of valence electrons from the transition metals prevent the lattice structures from being squeezed together, both of which enhance the resistance of the structures against large plastic (bulk and shear) deformations and lead to increased hardness. So far many transition-metal boride, carbide and nitride compounds have been successfully synthesized, including OsB_2[2,3], ReB_2[4–12], RuB_2[8], PtN[13], IrN_2[14], Ta_2N_3[15], Re_2C[16,17], Re_2N[18], Re_3N[18] and WB_4[8,19], to mention a few. Most of them are ultra-incompressible materials with bulk moduli ranging from 360 to 430 GPa,[8,14,16,18] which are close to that of diamond (440 GPa). However, their Vickers hardness measured in the asymptotic region independent of loading forces ranges from 15 to 30 GPa[3,8,9,17], which are much lower than that of diamond (80$\sim$100 GPa). One obvious explanation for the weaker Vickers hardness of the transition-metal boride, carbide and nitride compounds comparing to that of diamond is that the covalent bonds between the transition metals and light covalent elements, such as Os-B, Re-B, Re-N, and Ir-N bonds, etc., are weaker than those between light covalent elements, such as C-C and B-N bonds, etc. There exists, however, another less obvious cause which can further reduce the shear strengths, and thus the hardness, of these materials. Calculations show that most of the synthesized transition-metal boride, carbide and nitride compounds have much larger Poisson's ratios, ranging from 0.2 to 0.4[19–24], which are several times that of diamond (0.07)[25]. Under Vickers hardness tests, apart from the shear deformation, the Vickers indentor also produces a high compressive pressure normal to the loading surface which can induce large lateral volume expansions in materials with large Poisson's ratios. These large lateral volume expansions

will further weaken the atomic bonds in addition to that caused by the shear deformation in the Vickers hardness tests. An accurate prediction is needed to closely examine the underlying atomistic mechanisms for the structural and mechanical response under various loading conditions, such as those during the Vickers indentation tests. It has important implications for further understanding and development of the ultra-incompressible and ultrahard materials in the broad class of transition-metal boride, carbide and nitride compounds.

To characterize the mechanical properties of the above-mentioned transition-metal boride, carbide and nitride compounds, we examine their stress-strain responses to establish their deformation modes on the atomic level and determine their strengths in different hardness testing processes. It is noted that different hardness tests impose distinct loads on samples. In scratching hardness tests, samples are subject to mainly a shear stress; meanwhile, in indentation hardness tests, multi-axial stresses exist beneath indenters with predominantly a shear stress component and a normal compressive pressure that can reach tens or even hundreds of gigapascals.[26,27] The limit of structural stability of the specimen in these hardness tests is closely related to its maximum shear strength, which precedes the initiation of cracks and dislocations that lead to plastic deformation. Recent advances in computation physics have made it possible to calculate directly the ideal shear strength of a perfect crystal,[28–42] i.e., the lowest shear stress peak at which a perfect crystal becomes mechanically unstable, that can be compared to the shear strength derived from nano-indentation measurements.[42] These ideal strength calculations, using accurate first-principles methods, also provide atomistic deformation patterns and full range stress-strain relations which offer key insights into the mechanisms responsible for the fracture modes at incipient plasticity.[43–48] It represents a significant advance in computational materials research despite that some aspects, such as the load-sensitive hardness or the indentation size effect, which mainly stems from the generation and propagation of dislocations and cracks under large indentation loading, are still beyond the available computing capacity. The ideal shear strength calculations can provide an estimation of the asymptotic (i.e., load independent) hardness by comparing the calculated ideal shear strength with those of benchmark materials, such as diamond and c-BN whose hardness are well established. However, most previous ideal shear strength calculations did not consider normal compressive pressure beneath the indenter,[28–38,41–48] which makes them appropriate primarily to describe the scratching hardness of materials where normal pressures on scratching surfaces are not high.

In this paper, we report first-principles calculations of the ideal shear strength of hexagonal rhenium boride, carbide and nitride compounds (Re, Re_3N, Re_2N, Re_2C, Re_2B and ReB_2) by fully incorporating the effect of normal compressive pressure beneath the (Vickers) indenter using a recently developed method which provides a more accurate description for materials under indentation hardness tests.[39,40] The high-density valence electrons in these materials behave like a low-compressibility liquid. It is difficult to compress their volumes by hydrostatic pressure, which results in their high bulk moduli. However, in indentation hardness tests the uniaxial normal compressive pressure beneath the indenter can cause a large lateral volume expansion of the valence electrons in these structures as indicated by their large Poisson's ratios[19–24]. We examine how this lateral expansion affects the mechanical strength under indentation of these compounds with different chemical elements and compositions.

II. II. COMPUTATION METHOD

The ideal shear strength calculations were carried out using the Vienna Ab-initio Simulation Package (VASP) code,[49] adopting the projector augmented wave (PAW) potentials[50] and generalized-gradient-approximation (GGA) for the exchange-correlation energy with a plane-wave basis set. The GGA-PBE exchange-correlation functional proposed by Perdew, Burke and Ernzerhof[51] was used. The total energy of the structure was minimized by relaxing the structural parameters using a conjugate gradient optimization method.[52] The total-energy and stress calculations used a hexagonal unit cell with space groups *P63/mmc* for Re, Re_2N, Re_2C, Re_2B, ReB_2 and $P\overline{6}m2$ for Re_3N (see Fig. 1). A $11 \times 11 \times 7$ (and $11 \times 11 \times 9$ for Re) Monkhorst-Pack[53] k-point grid and a 700 eV energy cutoff were used in the calculations. The k-point sampling convergence was tested for both $11 \times 11 \times 7$ and $16 \times 16 \times 12$ Monkhorst-Pack k-point grids. The energy convergence of the calculation is on the order of 1 meV per atom, with the residual stresses in the fully relaxed structures less than 0.1 GPa. The quasistatic ideal indentation strength and relaxed loading path were determined using a method described previously,[39,40] in which the lattice vectors were incrementally deformed in the direction of applied shear strains, say ϵ_{xz}. At each step, the applied shear strain is fixed which determines the calculated shear stress σ_{xz}, while the other five independent components of the strain tensors and all the atoms inside the unit cell were simultaneously relaxed until (i) the compressive pressure (σ_{zz}) beneath the indentor normal to the chosen shear deformation plane reaches a specified value (i.e. $\sigma_{zz} = \sigma_{xz} tan\Phi$, where Φ is the centerline-to-face angle of the Vickers indenter), (ii) all the other four components (i.e. σ_{xx}, σ_{yy}, σ_{xy}, and σ_{yz}) of the Hellmann-Feynman stress tensor are negligibly small (less than 0.1 GPa), and (iii) the force on each atom becomes negligible (less than 0.001 eV/Å). The shape of the (deformed) unit cell, the positions of the atoms and the relation between the shear stress σ_{xz} and shear strain ϵ_{xz} are determined completely at each step by this constrained atomic relaxation, including the effect

of the normal compressive pressure σ_{zz}. The lowest peak stress in all the indentation shear directions determines the ideal indentation strength of the structure, at which the crystal structure starts to destabilize. If we set $\Phi = 0$ (so $\sigma_{zz} = 0$) in the calculation, it is equivalent to require that all the five stress components (except σ_{xz}) become negligible during the structural relaxation, which is the relaxation procedure used in the previous calculations of pure ideal shear stresses[28–38,41–48] that neglect the effects of the normal compressive pressure and geometry (indenter angles) of the indenter. Our test calculations for the lattice vectors of the equilibrium structure of Re, Re_3N, Re_2N, Re_2C, Re_2B and ReB_2, their bulk moduli and Poisson's ratios are given in Table I, which agree well with the previous calculation results[19,21–24,54,55]. The bulk moduli are obtained by fitting the energy-volume curves near the equilibrium structures to the Murnaghan equation, and the Poisson's ratios are evaluated from the calculated elastic constants.[22]

III. III. RESULTS AND DISCUSSIONS

We first present our calculated results by listing in Tables II, III and IV the calculated peak stresses and the corresponding strains at which the peak stresses appear in various tensile, pure shear and (Vickers) indentation shear deformation directions for Re, Re_3N, Re_2N, Re_2C, Re_2B and ReB_2. In Fig. 1, we plot the calculated stress-strain curves in the weakest direction under (a) tensile, (b) pure shear and (c) (Vickers) indentation shear deformation. Also shown [in Fig. 1(d)] is a comparison between the stress-strain curves under pure and (Vickers) indentation shear deformations for ReB_2 and Re_2C in their weakest indentation shear directions. From these results, it is clear that the [110] is the weakest tensile direction for all the hexagonal rhenium boride, carbide and nitride compounds studied here, while their weakest directions under pure shear and (Vickers) indentation shear are either $(001)[1\bar{1}0]$ or $(1\bar{1}0)[001]$. The lowest pure shear stress peaks (i.e., the ideal pure shear strength) and the lowest (Vickers) indentation shear stress peaks (i.e., the ideal indentation strength) of Re_3N (16.1 GPa and 15.1 GPa) and Re_2N (15.8 GPa and 15.6 GPa) are about the same, while those of Re_2B (19.4 GPa and 16.3 GPa) and ReB_2 (35.3 GPa and 27.6 GPa) show large differences. These results indicate that when the compositions of the light elements (B, C, N) reach a critical level to form covalent bonds among themselves, the strength of the rhenium boride, carbide and nitride compounds increases considerably. Otherwise their strengths are not very sensitive to the composition of the light elements, although the values are much higher than that of pure Re (10.9 GPa and 8.0 GPa). Compared to Re_2B and Re_2N, Re_2C exhibits much higher ideal pure shear and indentation strength (27.2 GPa and 22.5 GPa). Among all the hexagonal rhenium boride, carbide and nitride compounds studied in the present work, ReB_2 shows the highest ideal pure shear and indentation strength. For most of the structures, their (Vickers) indentation strengths are much lower than their ideal pure shear strengths, with the stress peaks appearing at smaller strains [see Fig. 1(d)]. Below we explain the physical mechanisms for these observations with an emphasis on the effect of normal compressive pressure beneath the indentor on the shear strength.

In Fig. 2, we compare the calculated total and partial density of stats (DOS) for Re_2B, Re_2C, and Re_2N at the equilibrium structure. The distributions of these total and partial DOSs are similar with the covalent bonds formed between the *d* electrons of Re and *p* electrons of B, C, and N. A pseudogap appears in all the DOS plots separating the bonding and anti-bonding states. The Fermi level of Re_2B (Re_2N) is lowered (pushed) into the bonding (anti-bonding) states, while the Fermi level of Re_2C is localized at the valley of its pseudogap. This shows that the structure of Re_2C is much more stable compared to those of Re_2B and Re_2N, which explains its high tensile, shear and indentation strength as shown in Tables II, III, IV and Fig. 1.

In Fig. 3, we compare the electron localization function (ELF), which gives a local measurement of electron paring[56], of Re_2B and ReB_2 at the equilibrium structures. Both the three-dimensional ELF isosurfaces (with ELF=0.71) and the two-dimensional ELF plots on a (110) crystalline plane passing through the labeled Re and B atoms show that covalent bonds between the B atoms in ReB_2 are much stronger than those between Re and B in Re_2B, which contributes to the greatly enhanced ideal shear and indentation strengths of the former as shown above.

We now discuss the effect of the normal compressive pressure beneath the (Vickers) indentor on the shear strength of ReB_2 and Re_2C, which have the highest ideal pure shear and indentation strength among all the hexagonal rhenium boride, carbide and nitride compounds studied here. From the results shown in Tables II, III, IV and Fig. 1, we can see that the pure shear direction $(1\bar{1}0)[001]$ of ReB2 is the weakest one, which has the lowest peak stress of 35.3 GPa at the shear strain ϵ=0.19. This peak stress determines the lowest shear stress needed to mechanically destabilize a perfect ReB2 crystal, that is, its ideal pure shear strength. When the normal compressive pressure beneath the Vickers indenter is included in the calculation, the weakest direction changes to $(001)[1\bar{1}0]$ with it peak stress reduced from 36.0 GPa to 27.6 GPa, which appears at a smaller shear strain ϵ=0.14 in the shear deformation process. The results in Fig. 1(d) show obvious weakening of the shear strength and early destabilization of ReB_2 structure induced by the normal compressive pressure beneath the indenter. To understand this normal pressure induced weakening in the indentation strength of ReB_2, we plot in Fig. 4 the three-dimensional ELF isosurfaces (with ELF=0.72) and the two-dimensional ELF plots on a (001) crystalline plane passing through the point at z=0

for ReB_2 at the equilibrium structure (ϵ=0) and at ϵ=0.14 under the pure shear (neglecting the normal compressive pressure) and (Vickers) indentation shear (including the normal compressive pressure) in the (001)[1$\bar{1}$0] direction, in which the (Vickers) indentation shear stress of ReB_2 reaches its peak at ϵ=0.14 [see Fig. 1(d)]. The B atoms in ReB_2 structure form buckled boron layers with opposite buckling directions in the layer at z=0 and z=c/2, respectively (see Fig. 4). The boron layers in ReB_2 are similar to the carbon layers in cubic diamond on its (111) crystalline planes. The boron layers in ReB_2 under the (001)[1$\bar{1}$0] shear will deform like those carbon layers in diamond (111) planes under the (111)[11$\bar{2}$] shear. Previous calculations[29,40] show that the shear directions (111)[11$\bar{2}$] and (111)[$\bar{1}$12] of diamond are not equivalent, with one direction easy to break the atomic bond in diamond (at the peak stress of 97 GPa) while the opposite direction hard to break these bonds (at the peak stress of 152 GPa). Similarly, here under the (001)[1$\bar{1}$0] shear, the atomic bonds in ReB_2 on the boron layer at z=0 are easy to break, while those on the boron layer at z=c/2 are hard to break. We focus our attention on the boron layer at z=0 where B atoms are labeled with numbers 1 through 8. From results in Fig. 4, we see that under the (001)[1$\bar{1}$0] pure shear at ϵ=0.14, the ELF isosurface with ELF=0.72 still exists in the middle of the atomic bond B_2-B_3 (and equivalently B_5-B_6, B_1-B_7, and B_4-B_8), indicating the covalent bonding nature of these bonds despite that the ELF isosurface starts to disperse into nearby B-Re bonds. While under the Vickers shear deformation in the same direction at the same strain, the ELF isosurface with ELF=0.72 disappears between atoms B_2-B_3, indicating the breaking of the covalent bonding between these atoms. The two-dimensional ELF plots on the (001) crystalline plane passing through the point at z=0 in Fig. 4 also show the same results that the ELF distribution between atoms B_2-B_3 (and equivalently B_5-B_6, B_1-B_7, and B_4-B_8) is much lower under Vickers shear than that under pure shear at ϵ=0.14 in the (001)[1$\bar{1}$0] shear direction. The bond length between atoms B_2-B_3 is 2.161 Å at ϵ=0.14 in Vickers indentation shear, while in pure shear at the same strain it is 1.946 Å. The lateral volume expansion caused by the normal compressive pressure beneath the indentor in indentation tests is responsible for this enhanced stretching of the strong covalent B-B bonds (B_2-B_3, B_5-B_6, B_1-B_7, and B_4-B_8), which significantly weakens the buckled hexagonal boron layer (at z=0) that is responsible for the high structural strength of ReB_2, as shown in Fig. 1(d). From results in Fig. 1(d) we also see that for ReB_2 at σ_{xz}=20 GPa, the stress-strain relations with and without normal pressure start to deviate from each other. The normal compressive pressure σ_{zz} ($\sigma_{zz} = \sigma_{xz} tan\Phi$ with Φ the centerline-to-face angle of the Vickers indenter) beneath the Vickers indenter at this stage is about 50 GPa, at which the indentation shear stress of ReB_2 starts to decrease relative to that of the pure ideal shear stress. It should be noted that the pressure distribution beneath the Vickers indenter is not uniform.[57] The maximum normal pressure P_{max} beneath the indenter can be several times higher than the average indentation pressure P_{ave}, which is obtained from the load divided by the indentation area. If we assume for simplicity that the pressure is linearly proportional to the indentation depth, we obtain P_{ave}=P_{max}/3 for the Vickers indenter. In such a case, the effect of normal compressive pressure on the ideal shear strength of ReB_2 would be relatively small when P_{ave} <16.7 GPa (P_{max} <50 GPa).

While the shear strength of ReB_2 under Vickers indentation decreases in all the shear directions, the indentation shear strength of Re_2C decreases in some directions, but in other directions it increases (see results in Table III and IV). To analyze these contrasting results, we plot in Fig. 5 the structural snapshots of Re_2C (a) under the (1$\bar{1}$0)[001] shear deformation in which at ϵ=0.125 the (Vickers) indentation shear stress-strain curve suddenly drops to zero [see Fig.1 (c)]; (b) under the (001)[1$\bar{1}$0] shear deformation in which at ϵ=0.15 the pure shear stress-strain curve suddenly drops to zero [see Fig.1 (b)]. The compressive pressure beneath the (Vickers) indentor reduces the indentation strength in the (1$\bar{1}$0)[001] shear deformation but enhances the indentation strength in the (001)[1$\bar{1}$0] shear deformation (see results in Table III and IV). The effect of the compressive pressure beneath the (Vickers) indentor on the shear strength of Re_2C can be explained by examining the behavior of the four Re atoms labeled 1 through 4 in Fig. 5. Under the (1$\bar{1}$0)[001] indentation shear deformation, when the strain $\epsilon \leq$0.125, the interatomic distances between Re_1-Re_4 and Re_2-Re_3 change continuously from 3.938 Å and 2.706 Å to 3.346 Å and 3.001 Å, respectively [see Fig.5 (a)]. With a small further increase in the shear strain (at ϵ=0.13), the normal compressive pressure beneath the indentor in the [1$\bar{1}$0] direction squeezes the Re_1 and Re_4 atoms, making them suddenly move closer which pushes the Re_2-Re_3 bond apart, forming a new Re_1-Re_4 bond. The interatomic distances between Re_1-Re_4 and Re_2-Re_3 at ϵ=0.13 change suddenly to 3.026 Å and 3.705 Å, respectively. However, under the (1$\bar{1}$0)[001] pure shear deformation, the Re_2-Re_3 bond is stable at ϵ=0.13 with a bond length of 2.961 Å which does not break until the shear strain reaches ϵ=0.17 [see Fig.1(c)]. The normal compressive pressure during the Vickers indentation causes an early break down of the Re_2-Re_3 bond and a reduction of 22.2% in the stress peak (indentation strength) in the (1$\bar{1}$0)[001] shear deformation. On the contrary, the effect of the normal compressive pressure beneath the indentor on the shear indentation strength of Re_2C is different in the (001)[1$\bar{1}$0] shear deformation. Under the (001)[1$\bar{1}$0] pure shear deformation, when the strain $\epsilon \leq$0.15, the interatomic distances between Re_1-Re_4 and Re_2-Re_3 change continuously from 3.938 Å and 2.706 Å to 3.529 Å and 3.142 Å, respectively [see Fig.5 (b)]. With a small further increase in the shear strain (at ϵ=0.155), the Re_2-Re_3 bond suddenly breaks apart which pushes Re_1 and Re_4 atoms moving suddenly closer, forming a new Re_1-Re_4 bond. The interatomic distances between Re_1-Re_4 and Re_2-Re_3 at ϵ=0.155 change suddenly to 2.789 Å and 3.932 Å, respectively. However under the (001)[1$\bar{1}$0] (Vickers) indentation shear deformation, the normal pressure

beneath the indentor in the [001] direction reduces the elongation of the Re_2-Re_3 bond due to the shear deformation and prevents it from breaking at ϵ=0.155. Under the (001)[1$\bar{1}$0] (Vickers) indentation shear deformation, when the strain ϵ $\leq$0.22, the interatomic distances between Re_1-Re_4 and Re_2-Re_3 change continuously from 3.938 Å and 2.706 Å to 3.804 Å and 2.844 Å, respectively [see Fig.5 (b)] with the stress peaks at ϵ=0.15. Under the (001)[1$\bar{1}$0] Vickers shear deformation, the stress peak (indentation strength) increases by 7.4% compared to that under pure shear deformation (see results in Table III and IV).

The effect of the normal compressive pressure on the shear strength of the rhenium boride, carbide and nitride compounds is much stronger compared to that on the traditional superhard materials. In Fig. 6 we plot the calculated stress-strain relations for the traditional superhard materials diamond and c-BN along their weakest shear directions under pure shear and Vickers indentation shear deformations. The results (see Fig. 1 and Fig. 6) show that the normal compressive pressure causes significant reductions in the indentation shear strength relative to the corresponding pure shear strength for the rhenium compounds (-23% for ReB_2 and -22% for Re_2C); in contrast, for the traditional superhard materials, the normal compressive pressure either causes a much smaller reduction in shear strength (-8.8% for c-BN) or even a slight enhancement (1.4% for diamond). The drastic reduction in indentation strength in the electron-rich transition metal (rhenium) boride, carbide and nitride compounds is attributed to the distinct bond deformation modes that include a large lateral volume expansion induced by normal pressure mediated by the high-density valence electrons in the transition metal (rhenium), which are absent in the traditional superhard materials. These high-density valence electrons behave like a low-compressibility liquid. It is difficult to compress their volume by hydrostatic pressures, which results in their high bulk moduli. However, in indentation hardness tests the uniaxial normal compressive pressure beneath the indentor causes a large lateral volume expansion of the valence electrons as indicated by their large Poisson's ratios (0.2 $\sim$ 0.3), which further weakens the atomic bonds in addition to that caused by the pure shear deformation. The effect of the normal compressive pressure beneath the indentor on the shear strength of the traditional superhard materials, such as diamond and c-BN, is much weaker due to their small Poisson's ratio (0.07 for diamond and 0.112 for c-BN). For materials with large Poisson's ratios, their pure ideal shear strengths (that is, the lowest peak stresses in the stress-strain curves) are expected to be low, as the peak stresses are generally determined by the initial derivatives (the shear moduli) of the stress-strain curves and it is already known that large Piooson's ratios reduce shear moduli.[1] The results in Table III show that the pure ideal strengths of rhenium boride, carbide and nitride compounds are much lower compared to those of diamond and c-BN given in Fig. 6. Furthermore, the results in Table IV indicate that there exists an additional weakening of the shear strengths of these rhenium compounds induced by the normal compressive pressures beneath (Vickers) indentors. The calculated stress-strain curves of ReB_2 and Re_2C in Fig. 1(d) illustrate that at small strains, the stress-strain curves are almost identical under both pure shear and (Vickers) indentation shear deformations. The effect of normal compressive pressures becomes strong only at large strains where the shear stresses and normal compressive pressures are large. These results indicate that the effect of strength weakening induced by the normal compressive pressures studied in the present work is not included in any hardness theory which adopts only physical quantities obtained at small strain limit, such as shear moduli *etc.* The relation between the reduction of indentation strength relative to that under pure shear deformations and Poisson's ratios in the rhenium boride, carbide and nitride compounds are not monotonic. This is because the Poisson's ratio describes the lateral expansion of a crystal under normal pressure near its equilibrium structure, while the indentation strength describes the response of a crystal at large deformation strains. For instance, although ReB_2 has a Poisson's ratio of 0.18 $\sim$ 0.20 that is smaller than that (0.292) of Re_2N, the indentation strength reduction of ReB_2 (23.2%) is much larger than that of the Re_2N (12.5%) (see Table IV). Even for Re_2C, which has a crystal structure very similar to that of Re_2N, its Poisson's ratio (0.252) and indentation strength reduction (22.2%) are not proportional to those of Re_2N. The indentation strength depends sensitively on the details of the crystal and electronic structures at large strains, which makes it difficult to predict accurately the indentation hardness from the properties obtained at equilibrium structures.[58]

IV. IV. CONCLUSIONS

In summary, we have established a comprehensive understanding of the stress-strain relation of several recently proposed ultra-incompressible hexagonal rhenium boride, carbide and nitride compounds under various loading conditions. Our calculations show that their ideal indentation strength under a Vickers indenter can be about 20% lower than their pure ideal shear strength. By comparing the calculated ideal indentation strength under the Vickers indenter among ReB_2 (27.6 GPa), Re_2C (22.5 GPa), c-BN (64.3 GPa) and diamond (97.6 GPa) (see Fig. 1 and Fig. 6), we estimate that the (asymptotic) Vickers hardness of ReB_2 and Re_2C are about 20-30 GPa and 15-25 GPa, respectively, which are consistent with the experimental results.[4,8,9,17] This explains the differences between the measured (asymptotic) Vickers hardness (20-30 GPa) of ReB_2 and the previous theoretical hardness predications (35-50 GPa) in which the normal compressive pressure beneath the indenter are neglected in the calculations.[58] The

higher pure shear ideal strength of ReB_2 (35.3 GPa) and Re_2C (27.2 GPa) suggests that they are suitable for applications in abrasive tools and wear-resistant coatings where compressive pressures normal to their scratching surfaces are not high. The large reduction of indentation strength in the rhenium boride, carbide and nitride compounds via lateral volume expansion is induced by the normal compressive pressure beneath the indenter. This distinct process is facilitated by the high-density valence electrons in these compounds that help transfer the normal compression to a lateral volume expansion. It increases the stretching of the atomic bonds in addition to that induced by the pure shear deformation and reduces the shear strength. This behavior is fundamentally different from those seen in the traditional superhard materials formed by light covalent elements (B, C, N) where the normal pressure beneath the indenter has less influence on their shear strength. The sensitive dependence of the shear strength of rhenium boride, carbide and nitride compounds on loading conditions also illustrates the difficulties to predict material hardness only from properties obtained at their equilibrium structures.

This work was supported by DOE Grant No. DE-FC52-06NA26274 at UNLV and NNSF of China Grant No. 11174200 at SJTU. H. Sun also appreciates the support of the Science and Engineering Interdisciplinary Research Foundation of SJTU.

---

* Corresponding author; Email:hsun@sjtu.edu.cn
† Corresponding author; Email:chen@physics.unlv.edu

[1] V. V. Brazhkin, A. G. Lyapin, and R. J. Hemley, Phil. Mag. A **82**, 231 (2002).
[2] R. B. Kaner, J. J. Gilman, and S. H. Tolbert, Science **308**, 1268 (2005).
[3] H. Y. Chung, J. M. Yang, S. H. Tolbert, and R. B. Kaner, J. Mater. Res. **23**, 1797 (2008).
[4] H. Y. Chung, M. B. Weinberger; J. B. Levine, A. Kavner, J. M. Yang, S. H. Tolbert, and R. B. Kaner, Science **316**, 436 (2007).
[5] J. B. Levine, S. L. Nguyen, H. I. Rasool, J. A. Wright, S. E. Brown, and R. B. Kaner, J. Am. Chem. Soc. **130**, 16953 (2008).
[6] H. Y. Chung, M. B. Weinberger, J. M. Yang, S. H. Tolbert, and R. B. Kaner, Appl. Phys. Lett. **92**, 261904 (2008).
[7] A. Latini, J. V. Rau, D. Ferro, R. Teghil, V. R. Albertini, and S. M. Barinov, Chem. Mater. **20**, 4507 (2008).
[8] Q. Gu, G. Krauss, and W. Steurer, Adv. Mater. **20**, 3620 (2008).
[9] J. Q. Qin, D. W. He, J. H. Wang, L. M. Fang, L. Lei, Y. J. Li, J. A. Hu, Z. L. Kou, and Y. Bi, Adv. Mater. **20**, 4780 (2008).
[10] S. N. Tkachev, J. B. Levine, A. Kisliuk, A. P. Sokolov, S. Q. Guo, J. T. Eng, and R. B. Kaner, Adv. Mater. **21**, 4284 (2009).
[11] J. B. Levine, S. H. Tolbert, and R. B. Kaner, Adv. Funct. Mater. **19**, 3519 (2009).
[12] N. Orlovskaya, Z. L. Xie, M. Klimov, H. Heinrich, D. Restrepo, R. Blair, and C. Suryanarayana, J. Mater. Res. **26**, 2772 (2011).
[13] E. Gregoryanz, C. Sanloup, M. Somayazulu, J. Badro, G. Fiquet, H. K. Mao, and R. J. Hemley, Nat. Mater. **3**, 294 (2004).
[14] A. F. Young, C. Sanloup, E. Gregoryanz, S. Scandolo, R. J. Hemley, and H. K. Mao, Phys. Rev. Lett. **96**, 155501 (2006).
[15] A. Zerr, G. Miehe, J. W. Li, D. A. Dzivenko, V. K. Bulatov, H. Hofer, N. Bolfan-Casanova, M. Fialin, G. Brey, T. Watanabe, and M. Yoshimura, Adv. Funct. Mater. **19**, 2282 (2009).
[16] E. A. Juarez-Arellano, B. Winkler, A. Friedrich, L. Bayarjargal, V. Milman, J. Y. Yan, and S. M. Clark, J. Alloys Compd. **481**, 577 (2009).
[17] Z. S. Zhao, L. Cui, L. M. Wang, B. Xu, Z. Y. Liu, D. L. Yu, J. L. He, X. F. Zhou, H. T. Wang, and Y. J. Tian, Cryst. Growth Des. **10**, 5024 (2010).
[18] A. Friedrich, B. Winkler, L. Bayarjargal, W. Morgenroth, E. A. Juarez-Arellano, V. Milman, K. Refson, M. Kunz, and K. Chen, Phys. Rev. Lett. **105**, 085504 (2010).
[19] M. Xie, R. Mohammadi, Z. Mao, M. M. Armentrout, A. Kavner, R. B. Kaner, and S. H. Tolbert, Phys. Rev. B **85**, 064118 (2012).
[20] Z. J. Wu, E. J. Zhao, H. P. Xiang, X. F. Hao, X. J. Liu, and J. Meng, Phys. Rev. B **76**, 054115 (2007).
[21] E. J. Zhao, J. P. Wang, J. Meng, and Z. J. Wu, J. Comput. Chem. **31**, 1904 (2010).
[22] J. B. Levine, J. B. Betts, J. D. Garrett, S. Q. Guo, J. T. Eng, A. Migliori, and R. B. Kaner, Acta Mater. **58**, 1530 (2010).
[23] H. Ozisik, E. Deligoz, K. Colakoglu, and G. Surucu, Phys. Status Solidi RRL **4**, 347 (2010).
[24] X. F. Hao, Y. H. Xu, Z. P. Li, L. Wang, F. M. Gao, and D. B. Xiao, Phys. Status Solidi B **248**, 2107 (2011).
[25] B. D. Fulcher, X. Y. Cui, B. Delley, and C. Stampfl, Phys. Rev. B **85**, 184106 (2012).
[26] Y. G. Gogotsi, A. Kailer, K. G. Nickel, Nature **401**, 663 (1999).
[27] K. J. Van Vliet, J. Li, T. Zhu, S. Yip, S. Suresh, Phys. Rev. B **67**, 104105 (2003).
[28] D. Roundy, C. R. Krenn, M. L. Cohen, and J. W. Morris Jr., Phys. Rev. Lett. **82**, 2713 (1999).
[29] H. Chacham and L. Kleinman, Phys. Rev. Lett., **85**, 4904 (2000).
[30] S. H. Jhi, S. G. Louie, M. L. Cohen, and J. W. Morris Jr., Phys. Rev. Lett. **87**, 075503 (2001).
[31] S. Ogata, J. Li, and S. Yip, Science **298**, 807 (2002).
[32] D. M. Clatterbuck, C. R. Krenn, M. L. Cohen, and J. W. Morris Jr., Phys. Rev. Lett. **91**, 135501 (2003).
[33] X. Blase, P. Gillet, A. S. Miguel, and P. Melinon, Phys. Rev. Lett. **92**, 215505 (2004).
[34] Y. Zhang, H. Sun, and C. F. Chen, Phys. Rev. Lett. **93**, 195504 (2004).
[35] Y. Zhang, H. Sun and C. F. Chen, Phys. Rev. Lett. **94**, 145505 (2005).

[36] M. G. Fyta, I. N. Remediakis, P. C. Kelires, and D. A. Papaconstantopoulos, Phys. Rev. Lett. **96**, 185503 (2006).
[37] R. F. Zhang, S. Veprek, and A. S. Argon, Appl. Phys. Lett. **91**, 201914 (2007).
[38] J. Yang, H. Sun, and C. F. Chen, J. Am. Chem. Soc. **130**, 7200 (2008).
[39] Z. C. Pan, H. Sun, and C. F. Chen, Phys. Rev. Lett. **98**, 135505 (2007); Phys. Rev. B **79**, 104102 (2009).
[40] Z. C. Pan, H. Sun, Y. Zhang and C. F. Chen, Phys. Rev. Lett. **102**, 055503 (2009).
[41] R. F. Zhang, Z. J. Lin, H. K. Mao, and Y. S. Zhao, Phys. Rev. B **83**, 060101 (2011).
[42] C. R. Krenn, D. Roundy, M. L. Cohen, D. C. Chrzan, and J. W. Morris Jr., Phys. Rev. B **65**, 134111 (2002).
[43] Y. Zhang, H. Sun and C. F. Chen, Phys. Rev. B **73**, 064109 (2006).
[44] Y. Zhang, H. Sun and C. F. Chen, Phys. Rev. B **73**, 144115 (2006).
[45] Y. Zhang, H. Sun and C. F. Chen, Phys. Rev. B **76**, 144101 (2007).
[46] Y. Zhang, H. Sun and C. F. Chen, Phys. Rev. B **77**, 094120 (2008).
[47] J. Yang, H. Sun and C. F. Chen, Appl. Phys. Lett. **94**, 151914 (2009).
[48] W. Zhou, H. Sun and C. F. Chen, Phys. Rev. Lett. **105**, 215503 (2010).
[49] See the web site: http://www.vasp.at/
[50] a) P. E. Blöchl, Phys. Rev. B **50**, 17953 (1994); b) G. Kresse and J. Joubert, Phys. Rev. B **59**, 1758 (1999).
[51] J. P. Perdew, K. Burke, and M. Ernzerhof, Phys. Rev. Lett. **77**, 3865 (1996).
[52] a) M. P. Teter, M. C. Payne, and D. C. Allan, Phys. Rev. B **40**, 12255 (1989); b) D. M. Bylander, L. Kleinman, and S. Lee, Phys Rev. B **42**, 1394 (1990).
[53] H. J. Monkhorst and J. D. Pack, Phys. Rev. B **13**, 5188 (1976).
[54] M. B. Lv, Y. Cheng, Y. Y. Qi, G. F. Ji, and C. G Piao, Physica B **407**, 778 (2012).
[55] X. P. Du, V. C. Lo, Y. X. Wang, J. Comput. Chem. **33** 18 (2012).
[56] a) A. D. Becke, K. E. Edgecombe, J. Chem. Phys. **92**, 5397 (1990); b) B. Silvi, A. Savin, Nature **371**, 683 (1994).
[57] A. L. Ruoff and H. A. Luo, J. Appl. Phys. **70**, 2066 (1991).
[58] A. Simunek, Phys. Rev. B **75**, 172108 (2007); *ibid* **80**, 060103 (2009).

Figures

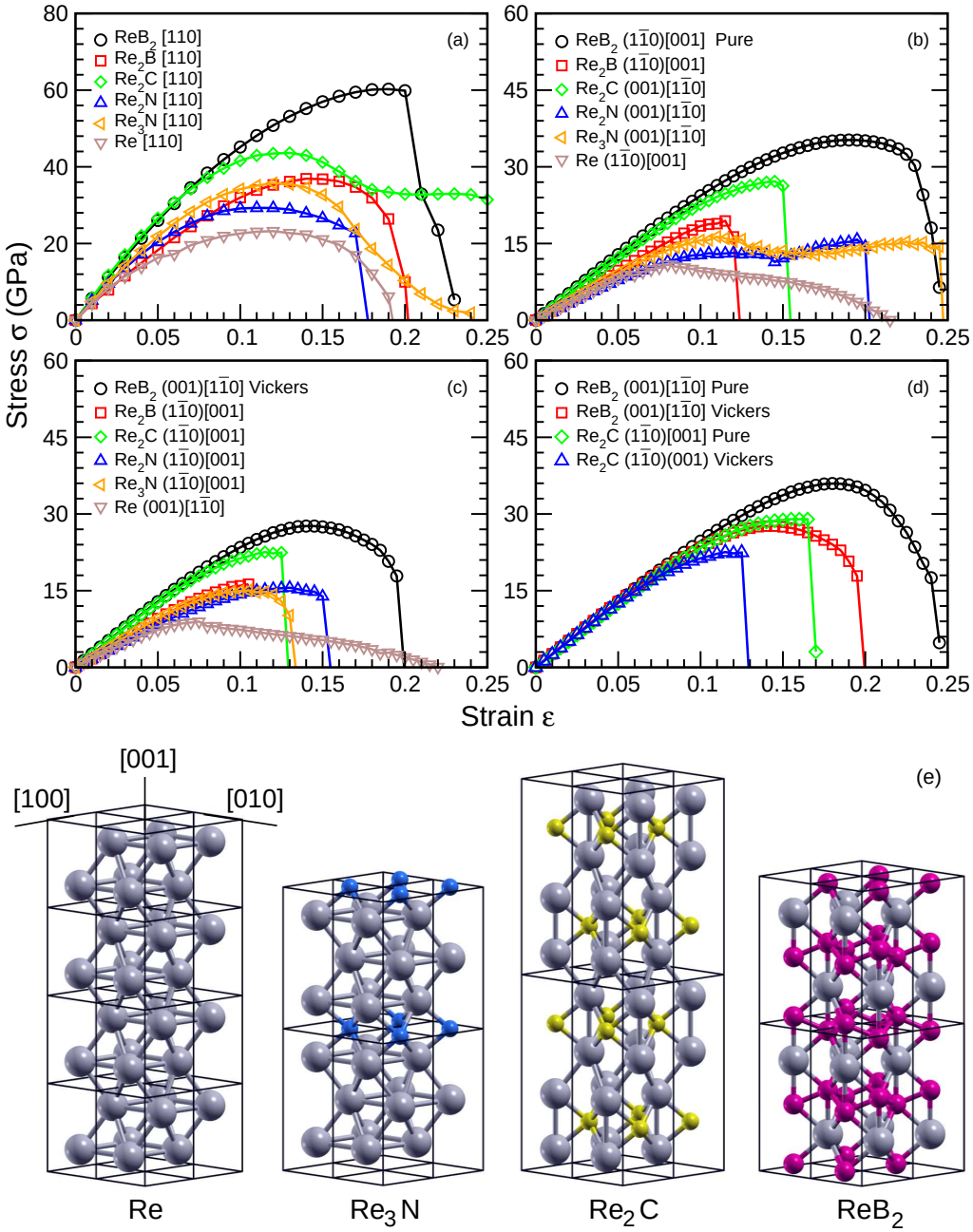

FIG. 1: (Color online) Calculated stress-strain curves in the weakest direction under (a) tensile, (b) pure shear and (c) Vickers shear deformation for Re, Re_3N, Re_2N, Re_2C, Re_2B and ReB_2. (d) Comparisons of the stress-strain curves under pure and Vickers shear deformations for ReB_2 and Re_2C in the weakest Vickers shear directions.

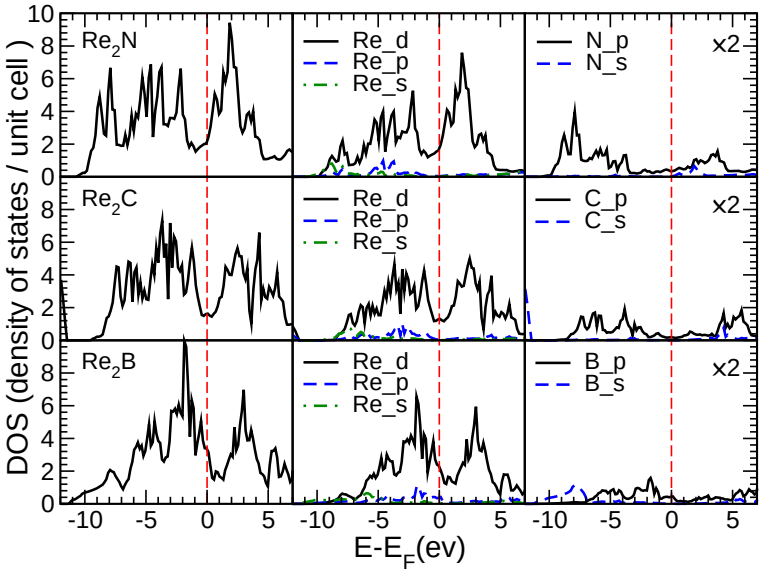

FIG. 2: (Color online) Calculated total and partial density of states (DOS) for Re_2B, Re_2C, and Re_2N at the equilibrium structure. The Fermi level is located at zero energy. The partial DOS of the N, C and B atoms are amplified by a factor of two.

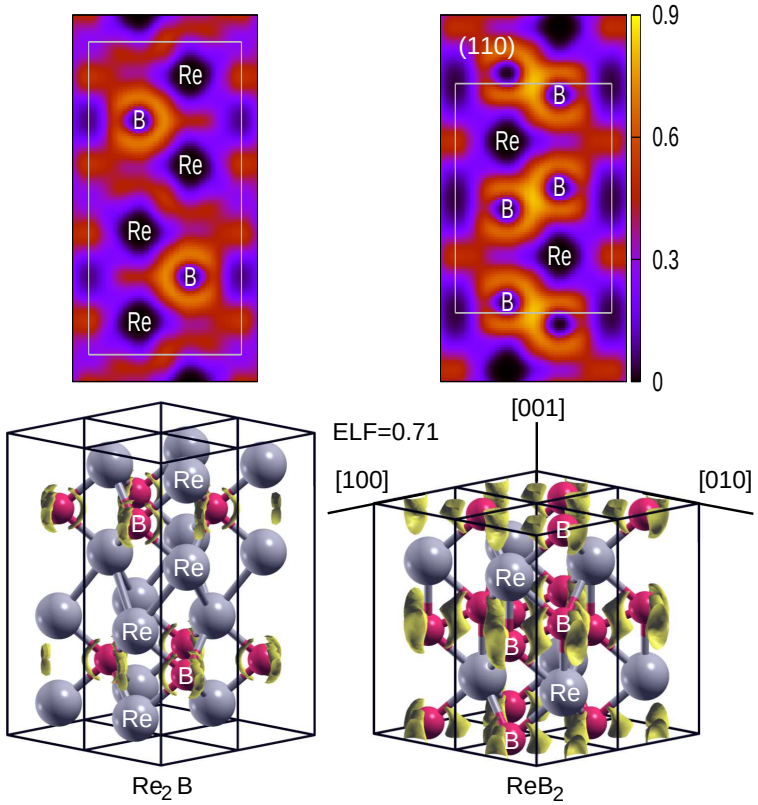

FIG. 3: (Color online) Calculated three-dimensional ELF isosurfaces (with ELF=0.71) and the two-dimensional ELF plots on a (110) crystalline plane passing through the labeled Re and B atoms in Re_2B and ReB_2.

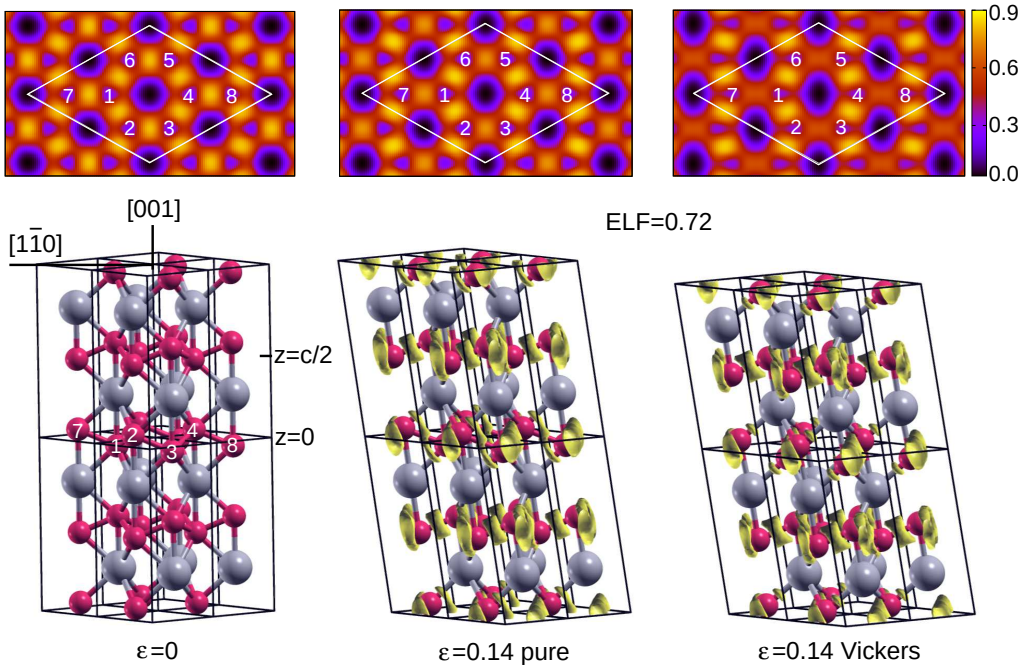

FIG. 4: (Color online) Calculated three-dimensional ELF isosurfaces (with ELF=0.72) and the two-dimensional ELF plots on a (001) crystalline plane passing through the point at z=0 for ReB_2 at the equilibrium structure (ϵ=0) and at ϵ=0.14, which is the strain corresponding to the peak stress under the Vickers shear for ReB_2 [see Fig. 1(c,d)], for the pure and Vickers shear in the (001)[1$\bar{1}$0] direction. The B atoms on the boron layer at z=0 are labeled with numbers 1 through 8.

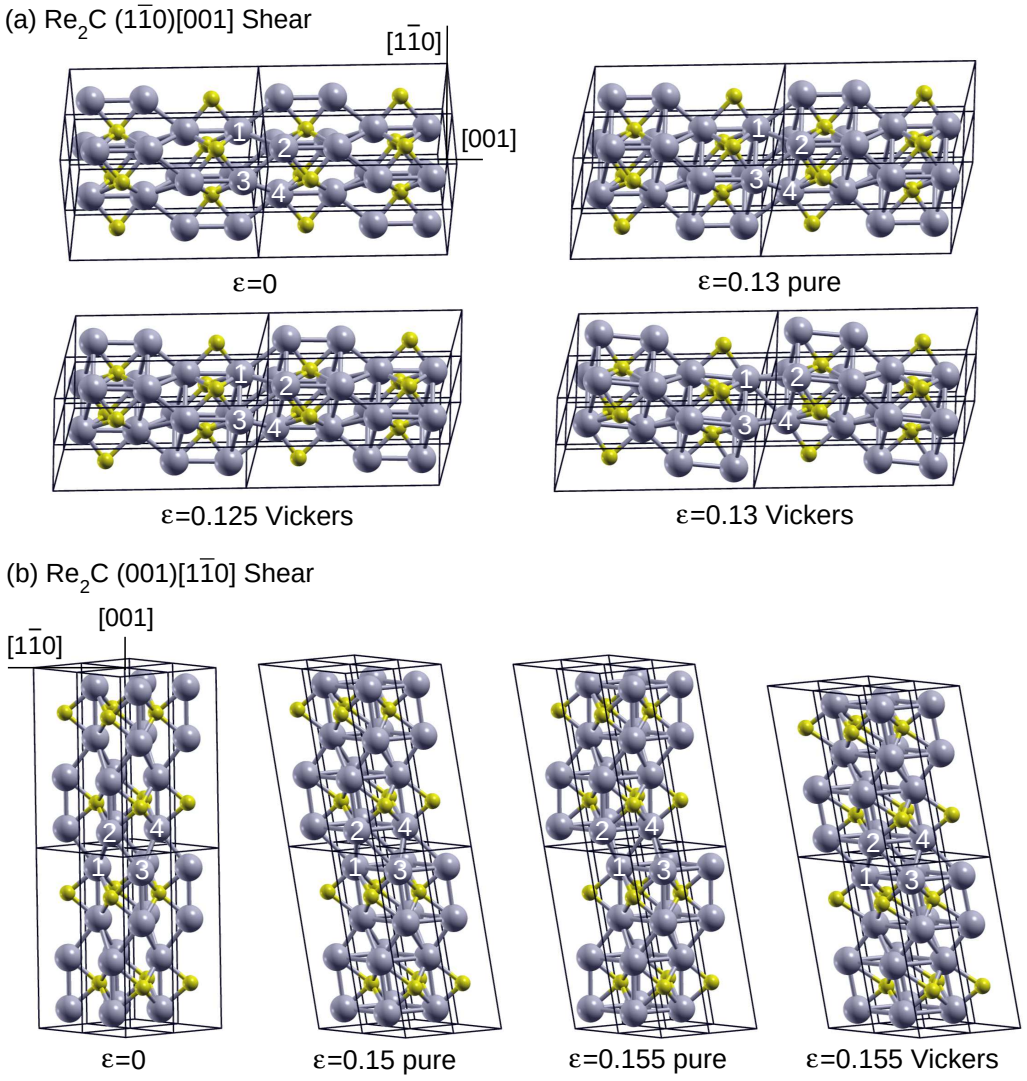

FIG. 5: (Color online) The structural snapshots of Re_2C (a) under the $(1\bar{1}0)[001]$ shear deformation in which at ϵ=0.125 the Vickers shear stress-strain curve suddenly drops to zero [see Fig.1 (c)]; (b) under the $(001)[1\bar{1}0]$ shear deformation in which at ϵ=0.15 the pure shear stress-strain curve suddenly drops to zero [see Fig.1 (b)].

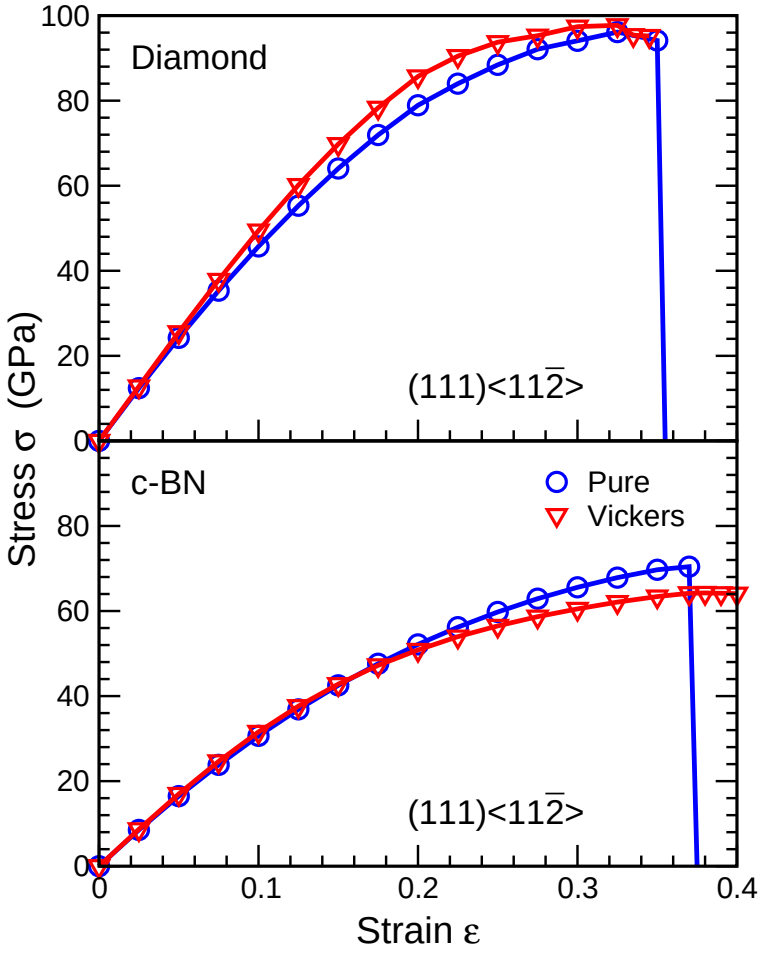

FIG. 6: (Color online) Calculated stress-strain relations for diamond and c-BN along their weakest shear directions under pure shear and Vickers indentation shear deformations.

Tables

TABLE I: The calculated lattice constants (a, c) in Å, bulk moduli (B) in GPa and Poisson's ratios (ν) for Re, Re_3N, Re_2N, Re_2C, Re_2B and ReB_2.

	Re	Re_3N	Re_2N	Re_2C	Re_2B	ReB_2
a	2.73	2.83	2.86	2.86	2.87	2.91
c	4.41	7.17	9.86	9.90	10.24	7.51
B	373.8	390.2	390.2	402.6	355.8	334.6
ν	0.313	0.284	0.292	0.252	0.271	0.184

TABLE II: The calculated peak stress (σ_{max}) in GPa and corresponding strain (ϵ_{max}) for Re, Re_3N, Re_2N, Re_2C, Re_2B and ReB_2 in various directions under tensile deformation.

	Re		Re_3N		Re_2N		Re_2C		Re_2B		ReB_2	
	ϵ_{max}	σ_{max}	ϵ_{max}	σ_{max}	ϵ_{max}	σ_{max}	ϵ_{max}	σ_{max}	ϵ_{max}	σ_{max}	ϵ_{max}	σ_{max}
[001]	0.200	55.6	0.150	59.5	0.180	58.6	0.130	57.6	0.190	48.8	0.190	94.1
[110]	0.130	23.3	0.120	35.7	0.110	29.3	0.130	43.6	0.140	36.9	0.190	60.3
[1$\bar{1}$0]	0.190	44.0	0.160	50.8	0.130	43.4	0.180	62.6	0.200	52.3	0.160	63.6

TABLE III: The calculated peak stress (σ_{max}) in GPa and corresponding strain (ϵ_{max}) for Re, Re_3N, Re_2N, Re_2C, Re_2B and ReB_2 in various directions under pure shear deformation.

	Re		Re_3N		Re_2N		Re_2C		Re_2B		ReB_2	
	ϵ_{max}	σ_{max}	ϵ_{max}	σ_{max}	ϵ_{max}	σ_{max}	ϵ_{max}	σ_{max}	ϵ_{max}	σ_{max}	ϵ_{max}	σ_{max}
(001)[110]	0.100	12.0	0.185	22.1	0.175	18.1	0.180	31.2	0.130	22.0	0.235	42.3
(001)[1$\bar{1}$0]	0.070	11.1	0.110	16.1	0.195	15.8	0.145	27.2	0.110	19.8	0.185	36.0
(110)[001]	0.110	16.4	0.195	23.7	0.250	23.2	0.200	34.3	0.135	23.3	0.245	43.5
(110)[1$\bar{1}$0]	0.200	20.9	0.195	31.2	0.165	26.5	0.215	40.0	0.240	31.6	0.275	52.4
(1$\bar{1}$0)[001]	0.080	10.9	0.230	17.8	0.220	17.8	0.155	29.0	0.115	19.4	0.190	35.3
(1$\bar{1}$0)[110]	0.185	16.3	0.180	25.4	0.150	22.0	0.195	32.3	0.225	25.3	0.190	35.3

TABLE IV: The calculated peak stress (σ_{max}) in GPa and corresponding strain (ϵ_{max}) in various directions under Vickers shear deformation, as well the change of the lowest peak stress under Vickers shear relative to that of pure shear in the same direction ($\Delta\sigma_{max} = (\sigma^V_{max} - \sigma^p_{max})/\sigma^p_{max}$) for Re, Re_3N, Re_2N, Re_2C, Re_2B and ReB_2.

	Re		Re_3N		Re_2N		Re_2C		Re_2B		ReB_2	
	ϵ_{max}	σ_{max}	ϵ_{max}	σ_{max}	ϵ_{max}	σ_{max}	ϵ_{max}	σ_{max}	ϵ_{max}	σ_{max}	ϵ_{max}	σ_{max}
(001)[110]	0.095	11.8	0.185	23.5	0.180	21.4	0.180	32.1	0.145	23.6	0.160	29.3
(001)[1$\bar{1}$0]	0.080	8.0	0.145	20.0	0.130	16.8	0.150	29.2	0.115	20.6	0.140	27.6
(110)[001]	0.105	11.6	0.140	17.2	0.160	16.6	0.135	24.5	0.130	16.9	0.170	34.2
(110)[1$\bar{1}$0]	0.130	12.0	0.150	20.2	0.145	18.6	0.160	26.2	0.175	19.2	0.185	32.7
(1$\bar{1}$0)[001]	0.075	9.0	0.105	15.1	0.130	15.6	0.115	22.5	0.105	16.3	0.180	34.8
(1$\bar{1}$0)[110]	0.090	16.8	0.100	31.0	0.090	28.2	0.125	36.4	0.115	24.7	0.175	35.2
$\Delta\sigma_{max}$	-27.6%		-15.3%		-12.5%		-22.2%		-16.2%		-23.2%	